# The flotation of magmatic sulfides transfers Cu-Au from magmas to seafloor massive sulfide deposits – Supplementary Information

Author 1: Aurélien Jeanvoine[1,2], corresponding author, aurelien.jeanvoine@gmail.com

Author 2: Jung-Woo Park[2]

Author 3: Ewan Pelleter[1]

Author 4: Antoine Bézos[3]

Author 5: Gilles Chazot[1]

Author 6: Jiwon Hwang[2]

Author 7: Yves Fouquet[1]

Affiliation 1: UMR6538 Geo-Ocean, IFREMER CNRS UBO UBS, Plouzané, France

Affiliation 2: School of Earth and Environmental Science, Seoul National University, Seoul, Republic of Korea

Affiliation 3: Nantes Université, Univ Angers, Le Mans Université, CNRS, Laboratoire de Planétologie et Géosciences, LPG UMR 6112, 44000 Nantes, France

16      **Supplementary Note 1:** Seafloor Massive Sulfide Deposits (SMS) Within the Fatu Kapa Area

17          The Fatu Kapa hydrothermal field comprises more than 40 SMS deposits spanning over an area of

18      about 10 km x 10 km at water depth ranging from 1300 to 2000 mbsl. Most of the deposits consist in small

19      (10 m x 10 m) chimney clusters. Less than ten SMS deposits have larger dimension (*i.e.*, > 100 m$^2$ up to

20      10,000 m$^2$). Chimneys are dominated by Zn-rich sulfides composed of sphalerite and wurtzite with minor

21      trace of pyrite, marcasite, chalcopyrite and rare silver-rich sulfosalts and native gold. Massive sulfides are

22      mainly composed of chalcopyrite and sphalerite/wurtzite. Sulfide ores are enriched in base metal

23      (Zn+Cu+Pb mean concentration = 17.7 wt.%) and in precious metal with gold and silver mean

24      concentrations at 9.1 ppm and 353 ppm, respectively (Supplementary Figure 1). Therefore, these deposits

25      display a geochemical signature that is closer to that of arc[1,2] or slab-coupled back-arc[1-3] deposits rather

26      than that of deposits associated with MORB[4,5] or slab-decoupled back-arc magmas[1,2,6].
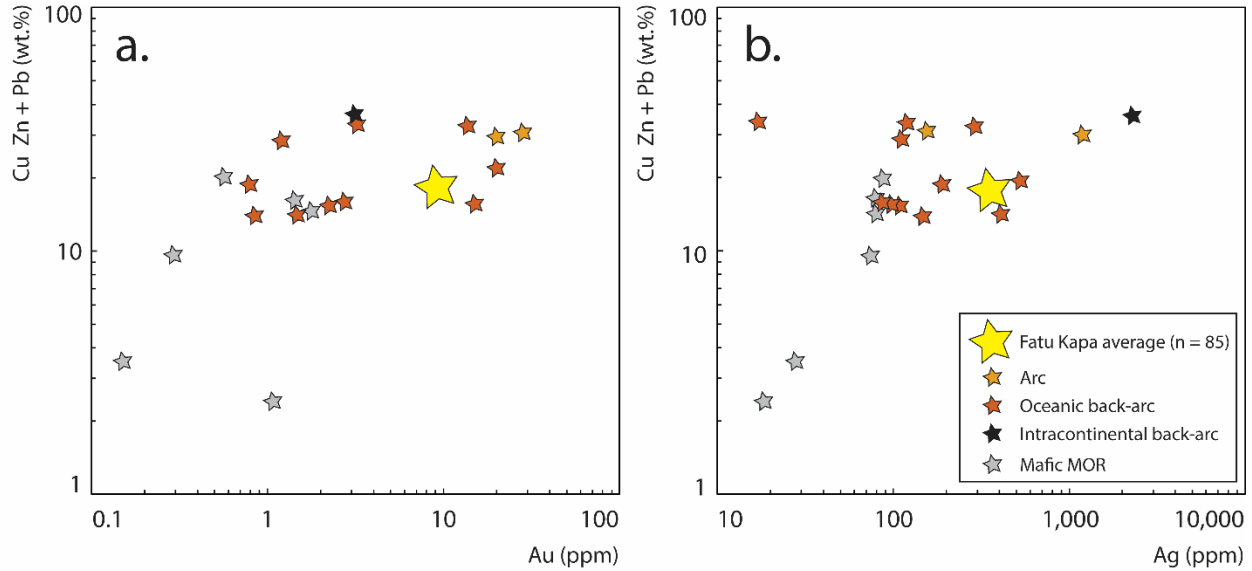


28      **Supplementary Figure 1:** Chart depicting the sum of Cu, Zn, and Pb concentrations as a function of the Au

29      (**a.**) and Ag (**b.**) concentrations of SMS deposits within the Fatu Kapa area. MOR: Mid-Ocean Ridge. "n"

30      stands for the number of X-ray fluorescence analyses conducted for each type of mineralization. Other

31    setting data are averaged values measured in hydrothermal deposits found in various geological settings.

32    The average concentration of base metals and Au in hydrothermal ores from the Fatu Kapa area falls

33    within the higher range of values observed in arcs and back-arc settings. The arc sites are sourced from

34    the Izu-Bonin arc (Myojin Knoll, Suiyo Knoll)[1,2]. The oceanic back-arc sites are associated with either slab-

35    decoupled MORB-like lavas from the Manus basin (Central Manus[1,2]), North Fiji basin (White Lady[6]), and

36    Mariana trough (18°N[1,2]), or with slab-coupled back-arc lavas from the Southern Lau back-arc basin (Vai

37    Lili[3], White Church[3], Northern Valu Fa Ridge[1,2], Central Valu Fa Ridge[1,2], and Southern Valu Fa Ridge[1,2]) and

38    the Manus back-arc basin (Pacmanus, SuSu Knoll[1,2]). The intracontinental back-arc site is from the Central

39    Okinawa trough[1,2]. Mafic MOR sites are from the East Pacific Rise (13°N[4]) and from the Mid-Atlantic Ridge[5]

40    (Menez Gwen, Lucky Strike, Trans-Atlantic Geotraverse, Snake Pit, Krasnov).

41
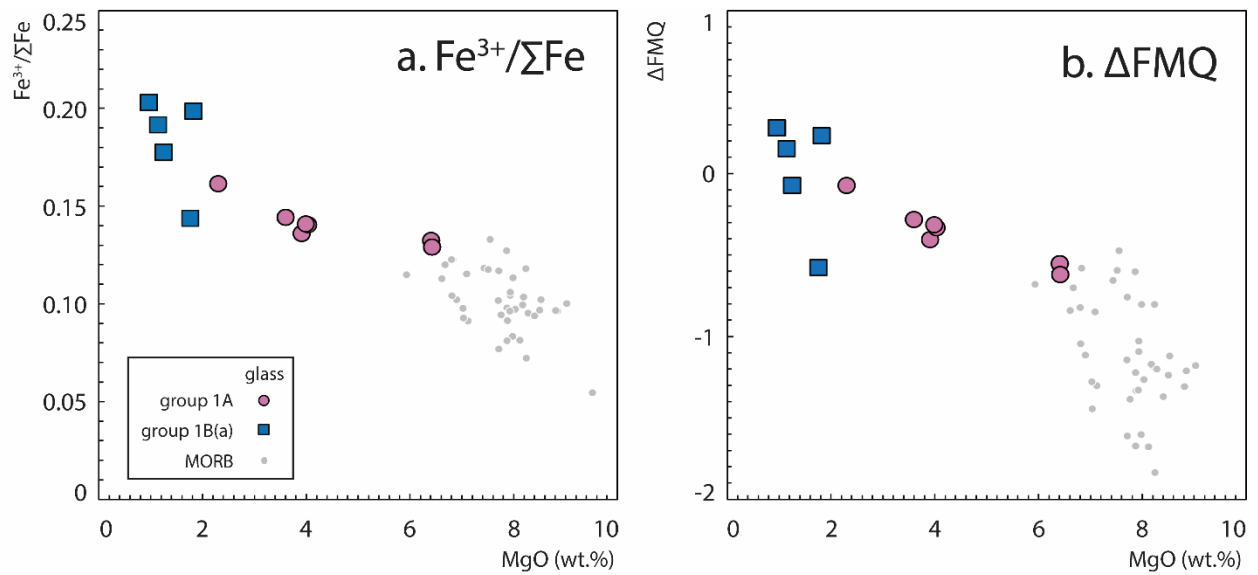
**Supplementary Figure 2:** Charts depicting $Fe^{3+}/\sum Fe$ ratio as a function of MgO (**a.**) and oxygen fugacity relative to the fayalite-quartz-magnetite (ΔFMQ) as a function of MgO (**b.**) compared to MORB[7,8]. ΔFMQ was estimated under atmospheric pressures and temperatures determined by thermohygrometry (Supplementary Figure 9) for Fatu Kapa magmas, and under atmospheric pressures and at a temperature of 1200°C for MORB.

47
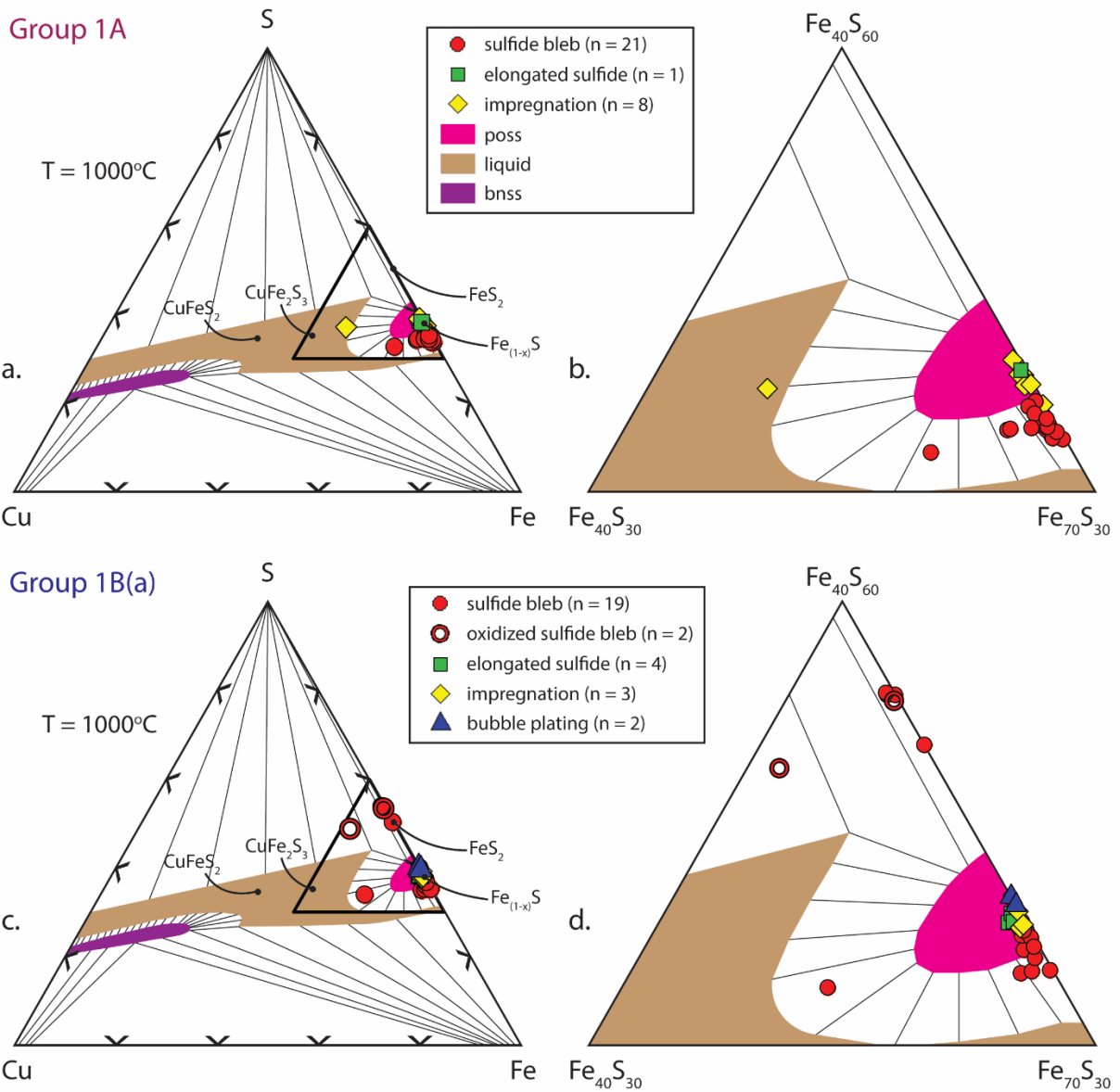
**Supplementary Figure 3:** Composition of sulfides identified within magmas from groups 1A and 1B(a) in

the Cu-Fe-S system at 1000°C[9]. **a.** Sulfides in group 1A lavas. poss: pyrrhotite solid solution; bnss: bornite

solid solution; $CuFeS_2$: chalcopyrite; $CuFe_2S_3$: cubanite; $FeS_2$: pyrite; $Fe_{(1-x)}S$: pyrrhotite, with x ranging from

0 to 1. Among sulfide blebs, only those with a total major element content exceeding 94 wt.% were

included. This filtering was made because significant sulfide bleb porosity (e.g., Supplementary Figure

4.a.d.), can result in a total major element content lower than 100 wt.%. **b.** Zoom of the area indicated by

54      the thick inner triangle in the diagram presented in a. The slight shifting of sulfide blebs toward the pure

55      iron endmember is an analytical artifact attributed to the major element total being less than 100 wt.%.
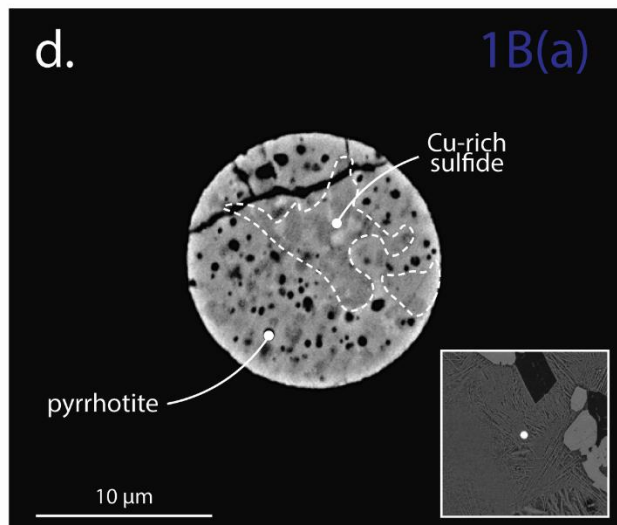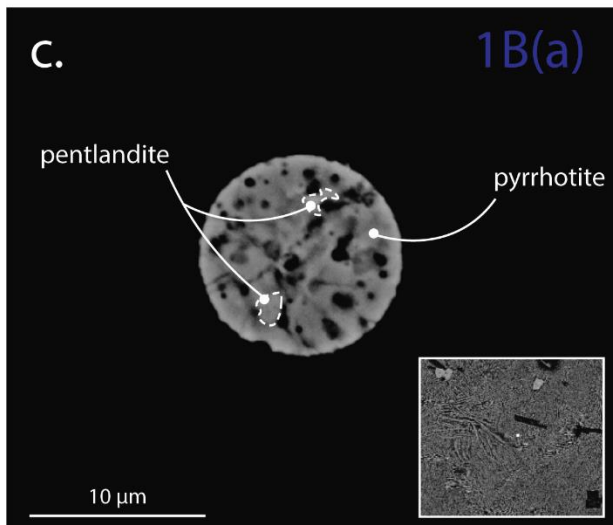
56      **c.** Sulfides in group 1B(a) lavas. **d.** Zoom of the area indicated by the thick inner triangle in the diagram

57      presented in c. Like group 1A sulfide blebs, only those with a total major element content exceeding 94

58      wt.% were selected, and the minor shift toward the pure iron endmember is attributed to the same

59      reasons as group 1A sulfide blebs.

a.  1A

pyrrhotite

5 μm

b.  1A

pyrrhotite

Cu-rich
sulfide

10 μm

c.  1B(a)

pentlandite

pyrrhotite

10 μm

d.  1B(a)

Cu-rich
sulfide

pyrrhotite

10 μm

e.  1B(a)

Ni-rich
pyrrhotite

50 μm

f.  1A

pyrrhotite

25 μm

60
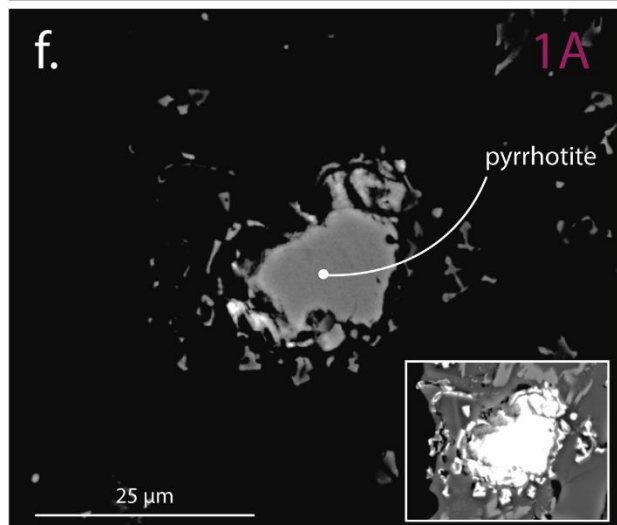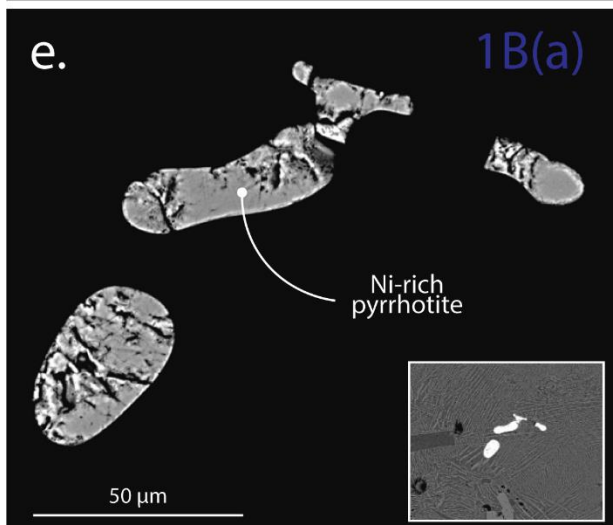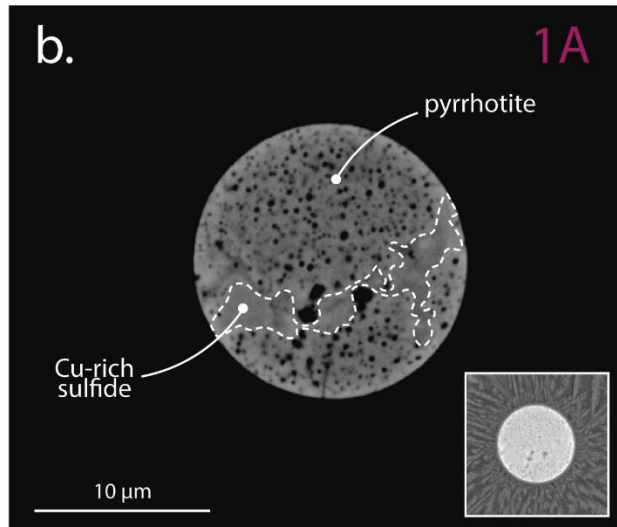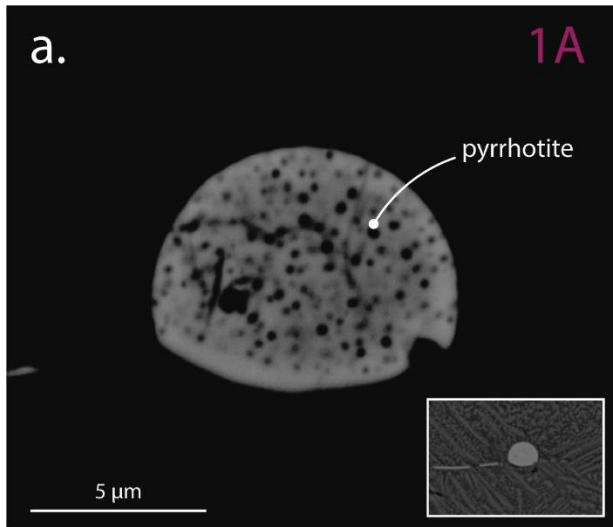
61 **Supplementary Figure 4:** Scanning electron microscope (SEM) images of individual sulfides identified

62 within group 1A and 1B(a). Insets feature SEM images of the same sulfide with varying luminosity and

63 contrast to emphasize the relationship between the sulfide and its surroundings. **a.** Sulfide bleb composed

64 of porous monosulfide solide solution (MSS) (sample FU3-DR01-08, group 1A, particle 510). **b.** Sulfide bleb

65 consisting of Cu-rich submassive sulfide between two porous MSS hemispheres (sample FU3-DR01-10,

66 group 1A, particle 35). **c.** Sulfide bleb primarily composed of porous MSS (sample FU3-DR03-05, group

67 1B(a), particle 252). Two inframicrometric Ni-rich phases (pentlandite) are identified. **d.** Sulfide bleb

68 displaying the same characteristics as b. (sample FU3-DR03-05, group 1B(a), particle 12). **e.** Elongated

69 sulfide composed of submassive MSS (sample FU3-DR03-05, group 1B(a), particle 230-231). **f.**

70 Impregnation resulting from the burst of one or several coalesced sulfide blebs, mainly composed of

71 submassive MSS (sample FU3-DR03-06, group 1A, particle 18). Micrometric Cu-rich phases are located at

72 the borders of the impregnation.

73
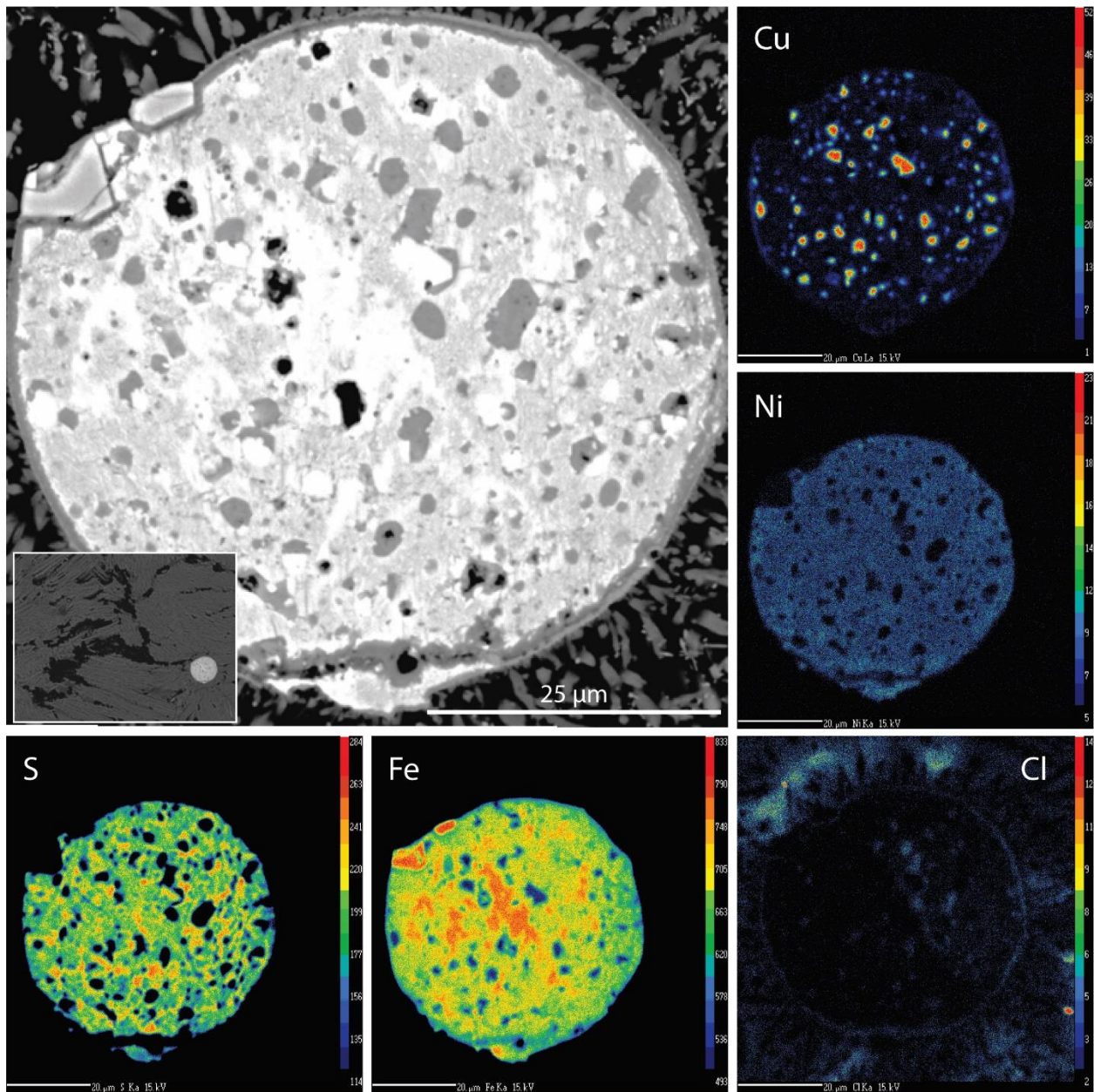
**Supplementary Figure 5:** SEM image and Electron Probe Microanalysis (EPMA) chemical mapping of a large sulfide bleb associated with a deformed bubble found in a group 1A lava (sample FU3-DR01-10, sulfide p251). The inset SEM image illustrates the relationship between the sulfide and the deformed bubble. The sulfide is primarily porous, consisting of approximately 85% MSS and 15% Cu-rich sulfide. The Cu-rich phases are located near the pores and sometimes penetrate them. Secondarily, the sulfide bleb

79   has undergone slight oxidation, as indicated by the strong, heterogeneous, and amorphous Fe signal.

80   Consequently, several pores become partially to completely filled with iron oxides. Chemical mapping

81   reveals that the pores filled with oxides exhibit a Cl signal, suggesting that oxidation is triggered by the

82   presence of aqueous fluids within the bubble.

83
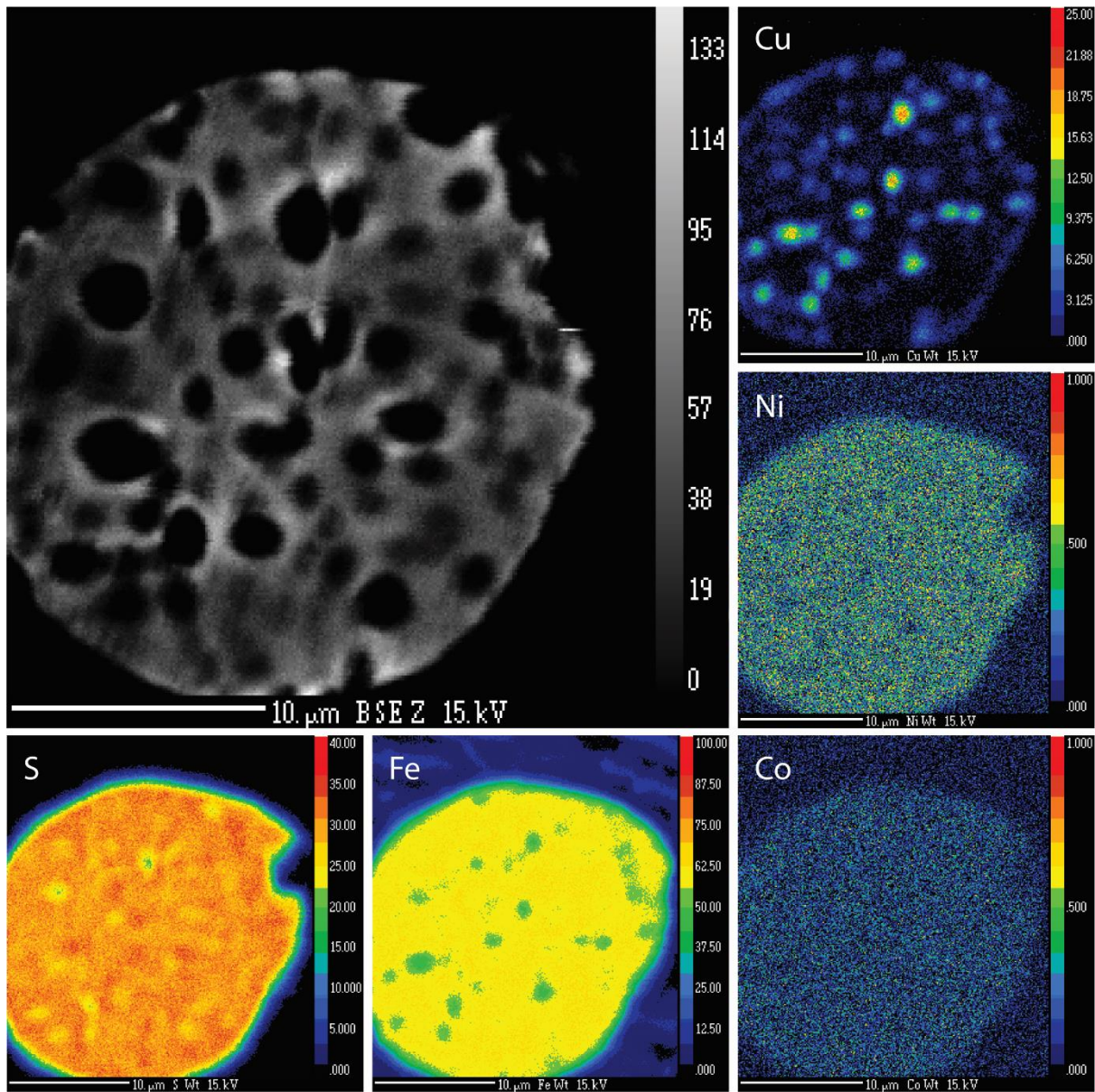
84

85    **Supplementary Figure 6:** SEM image and EPMA chemical mapping of a sulfide bleb found in a group 1A

86    lava (sample FU3-DR01-10, sulfide p341). Notably, the Cu-rich phases are consistently situated near the

87    pores within the sulfide.

88
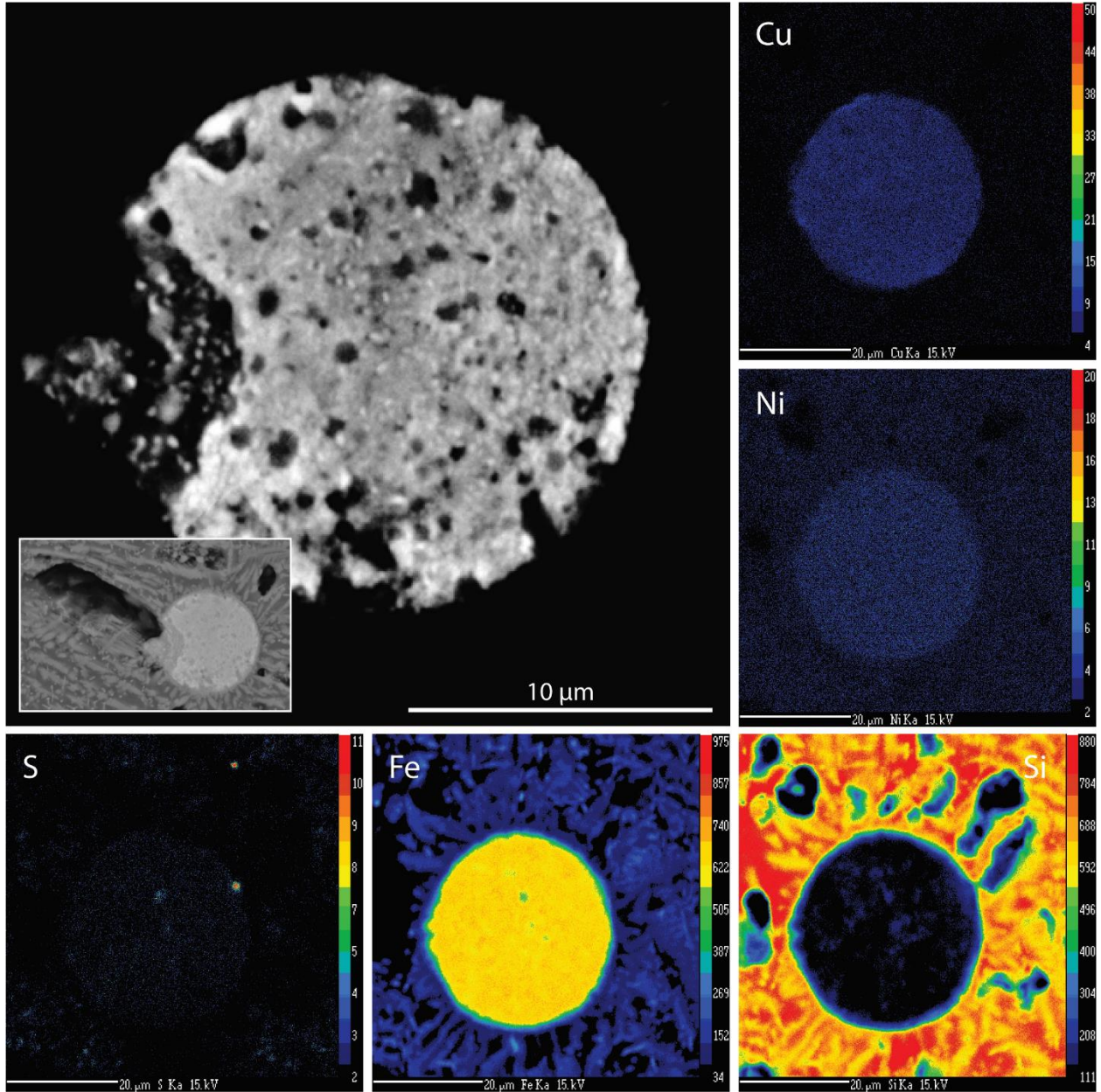
90     **Supplementary Figure 7:** SEM image and EPMA chemical mapping of a completely oxidized sulfide found

91     alongside a pocket of aqueous fluid in a group 1A lava (sample FU3-DR01-10, sulfide p175). The oxidation

92     process has resulted in the depletion of most of the S, Cu, and Ni content from the sulfide bleb.

93 **Supplementary Note 2:** Selection Criteria for Clinopyroxenes and Plagioclases in Establishing

94 Thermodynamic Constraints for Fatu Kapa Magmas

95       To determine the thermodynamic properties of the silicate melt, including temperature, pressure,

96 and water content, we used homogeneous and euhedral silicate minerals (clinopyroxenes and

97 plagioclases) (e.g., Supplementary Figure 8.a.b.). While most of these silicates are phenocrysts, in cases

98 where phenocrysts are rare or absent in certain lavas, we used smaller but still non-microlithic minerals.

99 For geometers requiring silicate melt composition in major elements, we mainly used whole rock data as

100 an approximation for the silicate melt, as there is minimal difference between whole rock and glass

101 analyses of major elements[10].

102       To ensure that the selected clinopyroxenes are in equilibrium with the silicate melt, we calculated

103 the observed Fe-Mg exchange coefficients between clinopyroxenes and the silicate melt ($Kd(Fe-Mg)_{cpx-}$

104 $_{SM}$)[11]. These values are then compared to the theoretical $Kd(Fe-Mg)_{cpx-SM}$, calculated using the equation

105 (35) from Putirka (2008)[12], with temperatures estimated through plagioclase thermohygrometry (the

106 reasons for this choice are developed in Supplementary Note 3). These temperatures are shown by the

107 small purple points in Supplementary Figure 9. Clinopyroxenes selected for thermobarometry are those

108 for which the observed $Kd(Fe-Mg)_{cpx-SM}$ fell within the range of theoretical $Kd(Fe-Mg)_{cpx-SM}$ ± 30% (brown

109 area in Supplementary Figure 8.c).

110       To ensure that the selected plagioclases are in equilibrium with the silicate melt, we calculated

111 the albite-anorthite exchange coefficients between plagioclases and the silicate melt ($Kd(Ab-An)_{pl-SM}$).

112 Typically, $Kd(Ab-An)_{pl-SM}$ values fall between 0.16 and 0.38 at temperatures above 1050$^o$C and between

113 0.05 and 0.15 for temperatures below this threshold[12]. The plagioclase thermometer applied to group 1A

114 magmas yields temperatures above 1050$^o$C, so we kept plagioclases with $Kd(Ab-An)_{pl-SM}$ values within the

115 range of 0.16 and 0.38 (brown area for 1A samples in Supplementary Figure 8.d). Contrarily, when we

116    apply the same thermometer to group 1B(a) magmas, it yields temperatures below 1050°C, and all

117    analysed plagioclases exhibit Kd(Ab-An)$_{pl-SM}$ values slightly above 0.15. Since most clinopyroxenes in group

118    1B(a) are unlikely in equilibrium with the silicate melt while the plagioclases are not, we decided to include

119    1B(a) plagioclases with Kd(Ab-An)$_{pl-SM}$ values ranging from 0.15 to 0.20 (grey rectangle in Supplementary

120    Figure 8.d) in our thermohygrometric calculations.
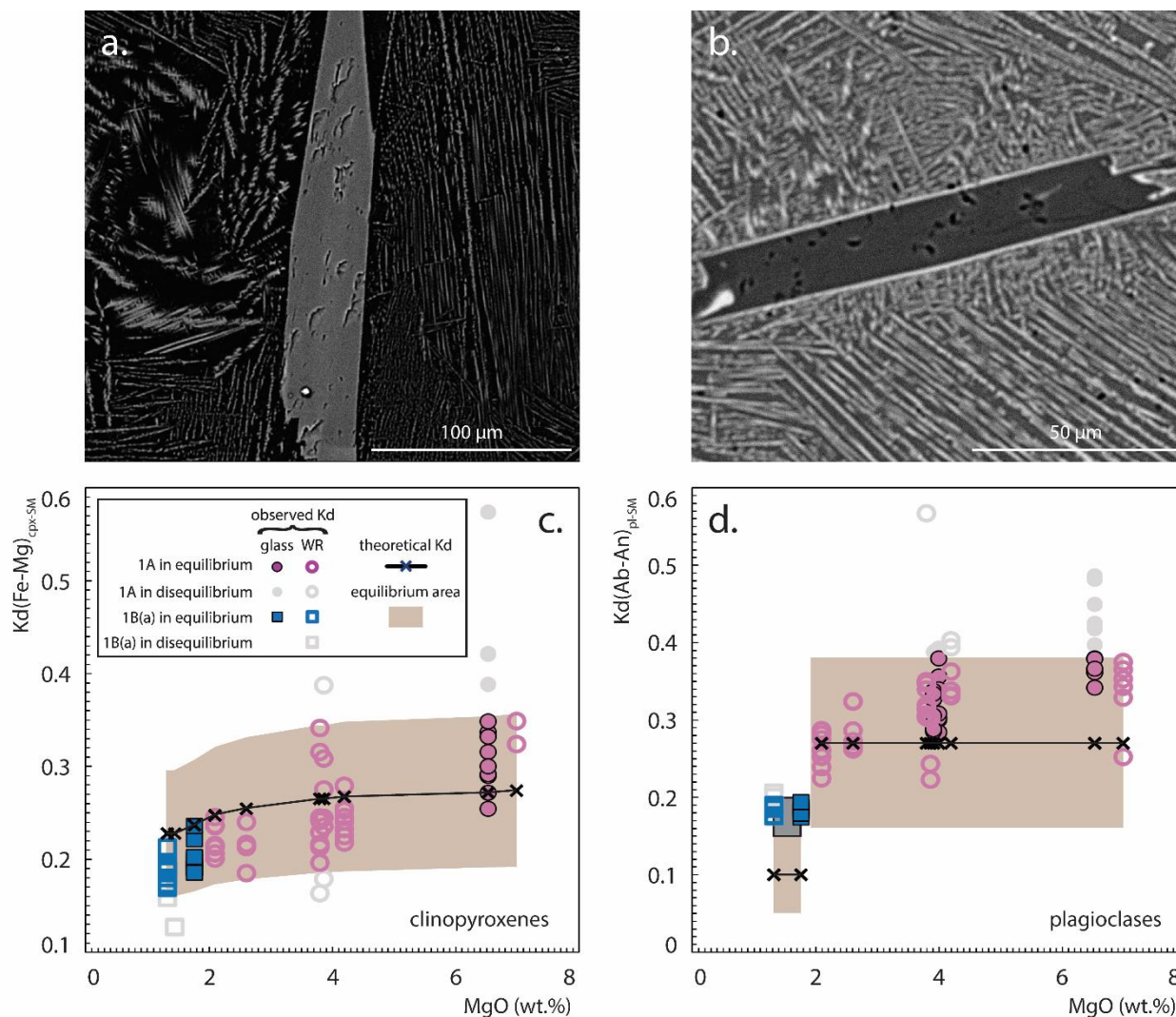
121



122    **Supplementary Figure 8:** Clinopyroxenes and plagioclases used for thermobarometry and

123    thermohygrometry. **a.** Example of a clinopyroxene phenocryst used for thermobarometry (sample FU3-

124    DR03-05, group 1B(a)). **b.** Example of a plagioclase phenocryst used for thermohygrometry (sample FU3-

125  DR03-05, group 1B(a)). **c.** Chart depicting the observed and theoretical Fe-Mg exchange coefficients

126  between clinopyroxenes and the silicate melt (Kd(Fe-Mg)$_{cpx-SM}$) as a function of MgO. WR (whole rock) and

127  glass refer to the type of data used when geometers require to input the major element content of the

128  silicate melt. Clinopyroxenes selected for thermobarometry are those for which the observed Kd(Fe-

129  Mg)$_{cpx-SM}$ fall within the range of the theoretical Kd(Fe-Mg)$_{cpx-SM}$ ± 30% calculated for a given sample

130  (brown area). Temperatures used to calculate theoretical Kd(Fe-Mg)$_{cpx-SM}$ are indicated in Supplementary

131  Figure 9. **d.** Chart depicting the observed and theoretical albite-anorthite exchange coefficients between

132  plagioclases and the silicate melt (Kd(Ab-An)$_{pl-SM}$) as a function of MgO. Plagioclases used for

133  thermohygrometry display observed Kd(Ab-An)$_{pl-SM}$ values that fall within the range of 0.16 to 0.38 (brown

134  area) for group 1A mafic to intermediate magmas and within the range of 0.15 to 0.20 (grey area) for

135  group 1B(a) felsic samples. Refer to Supplementary Note 2 for more details.

136    **Supplementary Note 3:** Chosen clinopyroxene thermobarometers and plagioclase thermohygrometer,

137    post-filtering for clinopyroxene thermobarometers and estimated temperatures and pressures.

138           The $H_2O$ content estimated with plagioclase thermohygrometers is a function of the plagioclase

139    and silicate melt composition in major elements, and to a lesser extent a function of pressure[12-14]. We

140    used the plagioclase-silicate melt thermohygrometer of Waters and Lange (2015)[14] to calculate the $H_2O$

141    content of Fatu Kapa magmas. This calculation was coupled iteratively with the temperature estimated

142    with the $H_2O$-dependant plagioclase-melt thermohygrometer given by the equation 25b of Putirka

143    (2008)[12]. For both group 1A and 1B(a) magmas, we adopted pressure values as the medians of the

144    pressures calculated with the clinopyroxene-silicate melt of Jorgenson et al. (2022)[15] (see below and

145    Supplementary Figure 9). A total of 57 out of 70 plagioclases measured were used for group 1A and a total

146    of 12 out of 14 for group 1B(a) (Supplementary Figure 8.c).

147           We tried three clinopyroxene thermobarometers: the clinopyroxene-only thermobarometers of

148    Wang et al. (2021)[16] and Jorgenson et al. (2022)[15] as well as the clinopyroxene-melt thermobarometer of

149    Jorgenson et al. (2022)[15]. The $H_2O$-dependant clinopyroxene-only thermobarometer of Wang et al.

150    (2021)[16] is based on an equation obtained by regression of a dataset of known temperature, pressure,

151    and water composition. We used the $H_2O$ content and temperatures obtained by plagioclase-silicate melt

152    thermohygrometry as input and, since the range of calibrated data extend from basalts to basalt-andesites,

153    we applied it to group 1A lavas only. The $H_2O$-independant clinopyroxene-only and clinopyroxene-silicate

154    melt developed by Jorgenson et al. (2022)[15] are based on machine learning algorithms rather than

155    equations obtained by regression of thermodynamic intensive values. A first advantage of algorithm-

156    based methods is that they are not restricted to a specific range of silicate melt compositions. A second

157    advantage is that they allow post-filtration of the calculated pressures and temperatures. Indeed, the

158    algorithm developed by Jorgenson et al. (2022)[15] runs 201 times and yields pressures and temperatures

159    as the averaged values of these runs. These output data are delivered with their respective interquartile

160    range (IQR), which is the difference between the third and the first quartile of the distributed pressure

161    and temperature runs. The closer the measured clinopyroxene is to one of the experiments used to train

162    the model, the lower the IQR. We therefore followed the recommendations of Jorgenson et al. (2022)[15]

163    in using only output data displaying an IQR lower than ~2 times the Standard Error Estimation (SEE) of the

164    models (Supplementary Table 1). A total of 42 over 49 clinopyroxenes measured were used for group 1A

165    and a total of 20 over 22 for group 1B(a) (Supplementary Figure 8.d).

166        For group 1A basalts, temperatures obtained with the two clinopyroxene-only thermobarometers

167    agree with each other, while those obtained with the plagioclase-melt thermohygrometer and those

168    obtained with the clinopyroxene-melt thermobarometer agree with each other but are 50$^{o}$C higher than

169    the other two (Supplementary Figure 9). We are confident on the reliability of whole rocks data as an

170    estimation of the silicate melt composition. Since adding silicate magma composition brings more

171    constraints on geo-thermometers, we think that the magmatic temperatures are best ascribed with the

172    clinopyroxene-silicate melt and the plagioclase-melt thermometers, although differences between

173    geothermometers get smaller with decreasing MgO. Therefore, group 1A basalts yield temperatures in

174    the range of 1140-1180$^{o}$C, while those for basalt-andesites are in the range of 1100-1145$^{o}$C and those for

175    andesites are in the range of 1060-1090$^{o}$C. For group 1B(a) magmas, temperatures obtained with the two

176    clinopyroxene thermobarometers are in agreement with each other but are ~60 to 80$^{o}$C higher than those

177    estimated with the plagioclase-silicate melt thermohygrometer. Both the albite-anorthite equilibrium for

178    plagioclases and the Fe-Mg equilibrium for clinopyroxenes that are used to determine temperatures are

179    a function of the $H_2O$ content of the silicate melt. However, for the clinopyroxene-only and clinopyroxene-

180    silicate melt thermobarometers developed by Jorgenson et al. (2022)[15], the water content of the silicate

181    melt is not considered. We estimated with the plagioclase thermohygrometers that the water content of

182  group 1B(a) magmas can reach up to ~2 wt.% (Figure 4). With the water dependant clinopyroxene-only

183  thermobarometer of Wang et al. (2021)[16], such water content difference yields a temperature difference

184  of ~60°C that is similar to the difference observed between plagioclase and clinopyroxene thermometers

185  applied to group 1B(a). Therefore, the plagioclase-melt thermometer is the only one yielding relevant

186  values for group 1B(a) magmas, and those temperatures are in the range of 980-1015°C.

187          Similarly to temperatures, pressures estimated with the clinopyroxene-only thermobarometers

188  are different than those estimated with the clinopyroxene-silicate melt thermobarometer

189  (Supplementary Figure 9). Here again, adding the silicate melt composition to geo-thermobarometry

190  brings more constraints to the estimated pressures, and we therefore chose the pressures estimated with

191  the clinopyroxene silicate-melt thermobarometer as the most representative for Fatu Kapa magmas at

192  depth. This pressure is constant from basalts to andesites of group 1A, with a median value of ~2.7 kbar

193  (red line in the 1A area of Supplementary Figure 9). Contrary to thermometers, barometers are not

194  significantly affected by $H_2O$ content, and we can therefore use the clinopyroxene-melt barometer of

195  Jorgenson et al. (2022)[15] to estimate pressures in group 1B(a) magmas. The pressure estimated for group

196  1B(a) magmas is lower than that estimated for group 1A magmas, with a median value of ~0.5 kbar (red

197  line in the 1A area of Supplementary Figure 9).

198  **Supplementary Table 1:** Characteristics of the plagioclase-silicate melt thermohygrometers and the

199  clinopyroxene(-silicate melt) thermobarometers applied to Fatu Kapa magmas. Pl: plagioclase; Cpx:

200  clinopyroxene; SM: silicate melt; T: temperature; P: pressure; B: basalt; BA: basalt-andesite; D: dacite; SEE:

201  standard error estimation; IQR max.: maximal interquartile range accepted; W&L15: Waters and Lange

202  (2015)[14]; P08: Putirka (2008)[12]; W21: Wang et al. (2021)[16]; J22: Jorgenson et al., 2022[15]. Characteristics of

203  the system that are not directly used in this study are indicated in grey.

| | Composition | H₂O SEE (wt.%) | T SEE (ºC) | T IQR max. (ºC) | P SEE (kbar) | P IQR max. (kbar) |
|---|---|---|---|---|---|---|
| Pl-SM W&L15 (H₂O) | B to D | 0.35 | 12 | - | - | - |
| Pl-SM P08 (T) | B to D | 1 | 36 | - | - | - |
| Cpx-only W21 (P) | B to BA | - | 36.6 | - | 1.68 | - |
| Cpx-only J22 (T, P) | - | - | 72.5 | 150 | 3.2 | 7 |
| Cpx-SM J22 (T,P) | - | - | 44.9 | 90 | 2.7 | 6 |

204



205
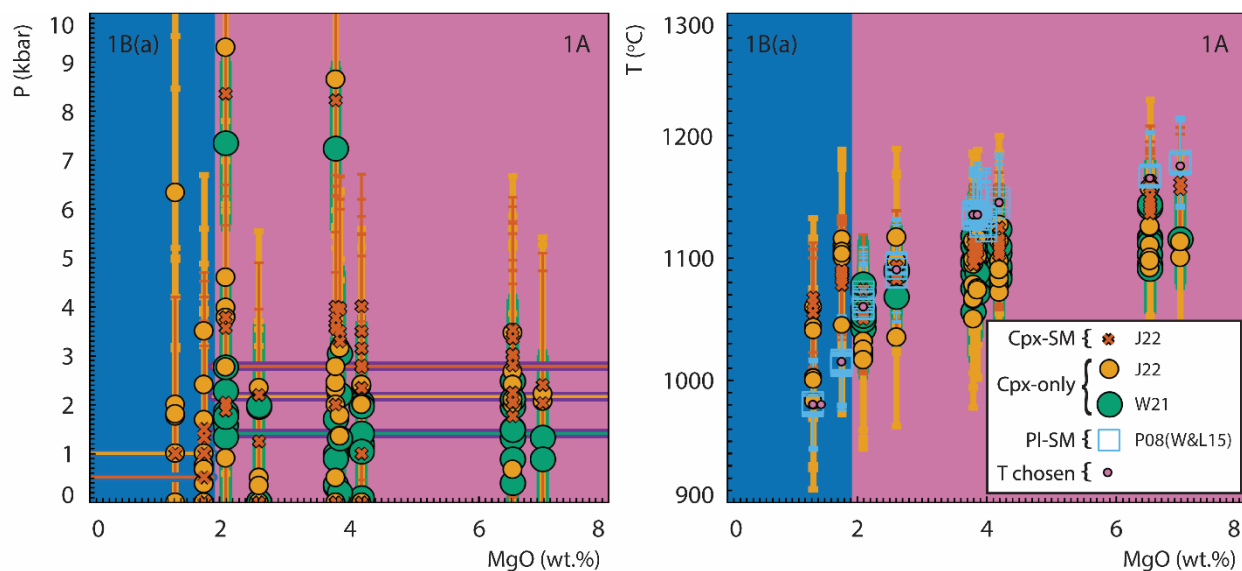
**Supplementary Figure 9:** Charts depicting the estimated pressures (left) and temperatures (right) calculated by thermobarometry and thermohygrometry for groups 1A and 1B(a) magmas as a function of MgO. Cpx-SM: clinopyroxene-silicate melt thermobarometer; Cpx-only: clinopyroxene-only thermobarometer; Pl-SM: plagioclase-silicate melt thermohygrometer; T: temperature. J22: Jorgenson et al. (2022)[15]; W21: Wang et al. (2021)[16]; P08(W&L15): Pl-SM thermometer of Putirka (2008)[12] incremented with the temperature-dependant hygrometer of Waters and Lange (2015)[14]. The uncertainties correspond to the SEE of each thermobaro(hygro)meter (Supplementary Table 1). 1A magmas display MgO values that are higher than 1.9 wt.% (pink area) while those of 1B(a) are lower than 1.9 wt.% MgO (blue area).

214 Red, yellow, and green lines in the MgO versus pressure plot correspond to the median values estimated

215 with the thermobarometers of J22 (Cpx-SM), J22 (Cpx-only) and W21, respectively, for groups 1A and

216 group 1B(a) magmas. Despite the high SEE, estimated pressures are not strongly widespread for each

217 group, and the median values estimated with both Cpx-SM and Cpx-only thermobarometers from J22 are

218 significantly lower for group 1B(a) than for group 1A. Temperatures of groups 1A and 1B(a) determined

219 with each thermobaro(hygro)meter are in good agreement with each other, although 1B(a) temperatures

220 estimated with the Pl-SM system are slightly lower than those estimated with the Cpx-SM and Cpx-only

221 systems. Refer to Supplementary Note 3 for more details.
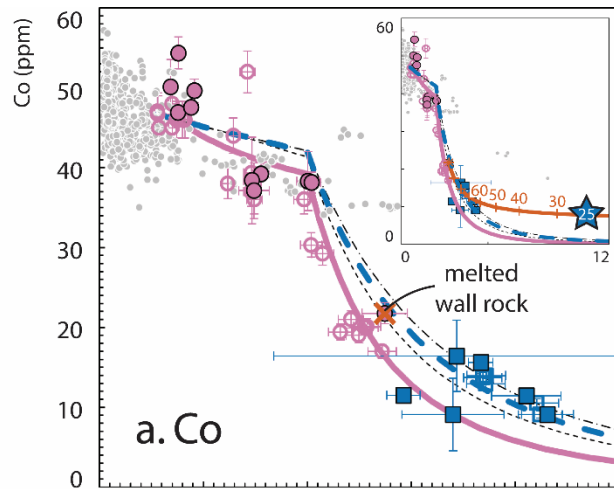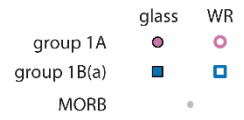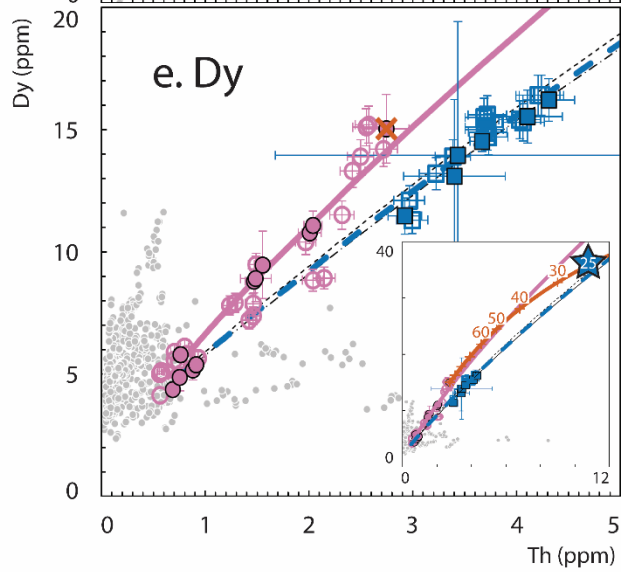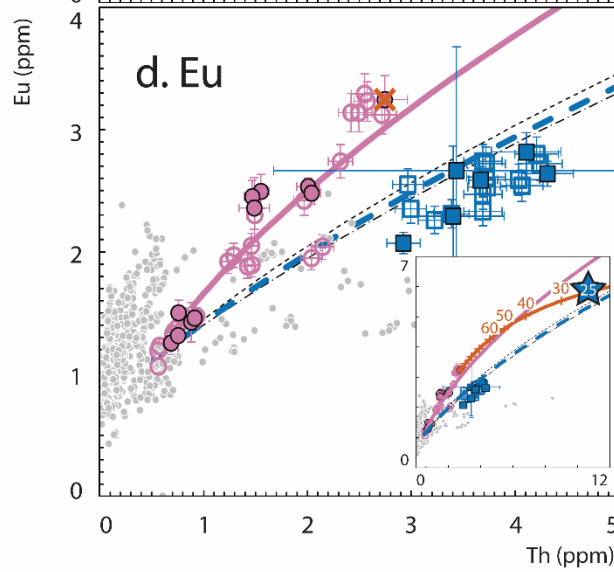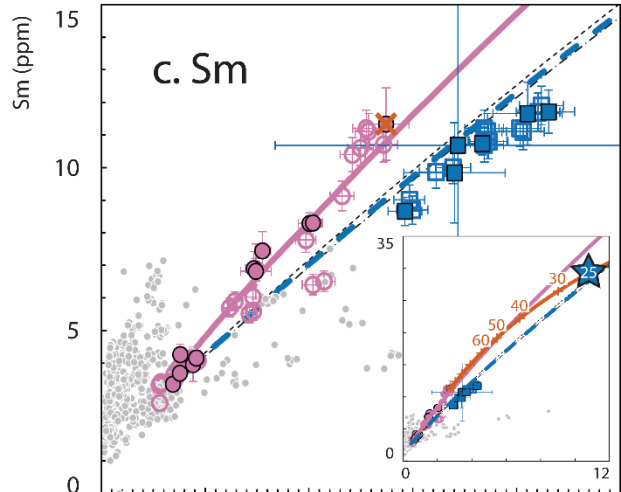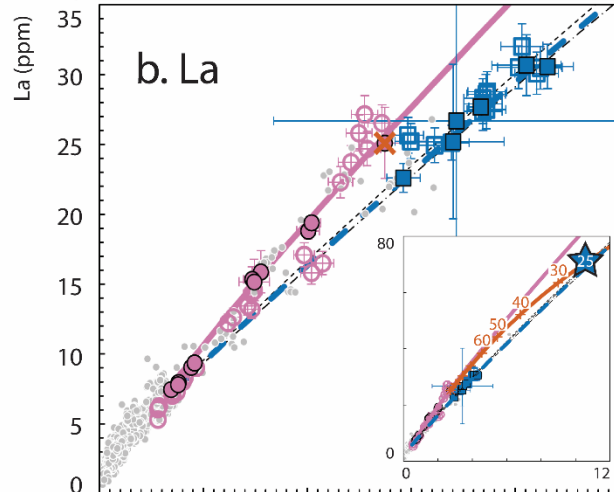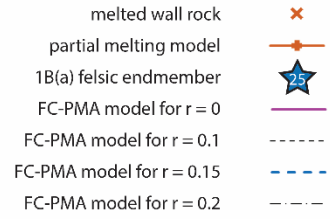
223    **Supplementary Figure 10:** Charts depicting Co (**a.**), La (**b.**), Sm (**c.**), Eu (**d.**), and Dy (**e.**) as a function of Th

224    for Fatu Kapa whole rocks (WR, open circles) and glasses (filled circles) in groups 1A (purple color) and

225    1B(a) (blue color). The uncertainties for are 5% of the measured value for whole rocks, and for glass

226    measurements they are provided at a 2-sigma level. These elements are used to determine the r value

227    because they are non- (REE) to moderately (Co) chalcophile and does not have an affinity for aqueous

228    fluids, so that they are not affected by other unknowns involved in the model, such as the proportion of

229    sulfides and aqueous fluids exsolved. A r value of 0.15 matches the Co and REE measured values. Refer to

230    Methods section for more details. Acronyms are the same as for Figure 1,5 (main). Numbers on the curve

231    refer to the partial melting degree (%) of the wall rock and the red star indicates the degree chosen for

232    modelling 1B(a) magmas, which is equal to 25%. Excluding Co, measured values are taken from Jeanvoine

233    et al. (2021)[10] and MORB concentrations are taken from Jenner and O'Neill (2012)[17]. The silicate minerals

234    – silicate melt partition coefficients of REE are taken from Ersoy et al. (2010)[18] and references therein. The

235    oxide – silicate melt partition coefficients of REE are taken from Wanless et al. (2010)[19] and references

236    therein. We assumed a value of 0.0001 for the monosulfide solid solution – silicate melt and sulfide liquid

237    – silicate melt partition coefficients for REE and we did not consider the partitioning of these non-volatile

238    elements into an aqueous fluid phase (partition coefficient equal to 0.0001). Partition coefficients used

239    for modelling the behavior of Co are indicated in Supplementary Table 5.

240

241    **Supplementary Table 2:** Composition of the initial melt used for modelling the behavior of 1A and 1B(a)

242    magmas, composition of the melted wall rock and composition of the resulting felsic magma that is mixed

243    with the initial magma during its evolution. It is important to note that due to the complexity and

244    numerous unknown factors influencing the behavior of highly chalcophile elements during partial melting,

245    we used the same Cu and Pd concentrations in the felsic endmember than in the melted wall rock.

246

| | Cu (ppm) | Pd (ppb) | Zn (ppm) | Pb (ppm) | Co (ppm) | Th (ppm) |
|---|---|---|---|---|---|---|
| Initial magma 1A and 1B(a) | 120.0 | 1.450 | 68.5 | 0.76 | 47.0 | 0.50 |
| Melted wall rock 1B(a) | 33.3 | 0.027 | 160.0 | 2.70 | 21.8 | 2.74 |
| Felsic endmember 1B(a) | 33.3 | 0.027 | 172.6 | 5.89 | 7.8 | 10.75 |

247

248 **Supplementary Table 3:** Parameters used for modelling the behavior of metals in group 1A by fractional

249 crystallization. Ol: olivine; Pl: plagioclase; Cpx: clinopyroxene; Ox: oxide; Fe-S: Cu-poor sulfides; Cu-Fe-S:

250 Cu-rich sulfides. In the mode column, numbers indicate the proportion (weight percent) of the associated

251 phase compared to the other phases that form at a given stage. When a sulfide phase is formed, the

252 proportion of Fe-S and Cu-Fe-S, expressed in percent, is indicated in brackets. The assimilated silicate melt

253 is formed by partial melting of a felsic lava from group 1A (sample FU3-DR13-05) whose mode is Ol5.2,

254 Pl43.8, Cpx38.8, Ox12.2[10].

| Group | Stage | Mode | $F_{PM}$ (%) | r | $H_2O$ added in the melted wall rock (wt.%) | Th value at VS (ppm) |
|-------|-------|------|--------------|---|---------------------------------------------|----------------------|
| 1A | 1 | Ol7.4, Pl41.6, Cpx48.3, Ox2.7 | - | - | - | - |
| | 2 | Ol7.4, Pl41.41, Cpx48.3, Ox2.7<br>Sulfide0.19 (Fe-S 15, Cu-Fe-S 85) | - | - | - | - |
| | 3 | Ol7.4, Pl41.41, Cpx48.3, Ox2.7<br>Sulfide0.19 (Fe-S 95, Cu-Fe-S 5) | - | - | - | - |
| | 4 | Ol5.2, Pl43.71, Cpx38.7, Ox12.2<br>Sulfide0.19 (Fe-S 95, Cu-Fe-S 5) | - | - | - | - |

255

256

257  **Supplementary Table 4:** Parameters used for modelling the behavior of metals in group 1B(a) magmas by

258  fractional crystallization coupled to partial melting and assimilation. As for group 1A magmas, sulfide

259  saturation is reached when the remaining melt fraction is equal to 70% of its initial volume. $F_{PM}$: rate of

260  partial melting; r: ratio between the rate of assimilation and the rate of fractional crystallization; $VS_x$:

261  volatile saturation, scenario x (with x from 1 to 4, see Figure 4 (main)); other abbreviations and

262  information are the same as in Supplementary Table 3. The modelling progresses from stage 1 to stage 4

263  unless Th values at the onset of VS (indicated in bold) are reached for a specific VS scenario. After reaching

264  this value, stages 5 begin.

| Group | Stage | Mode | $F_{PM}$ (%) | r | $H_2O$ added in the melted rock (wt.%) | Th value when the stage starts ppm |
|---|---|---|---|---|---|---|
| 1B(a) | 1 | Ol7.4, Pl41.6, Cpx48.3, Ox2.7 | 25 | 0.15 | - | 0.50 |
| | 2 | Ol7.4, Pl41.41, Cpx48.27, Ox2.7 Sulfide0.22 (Fe-S 10, Cu-Fe-S 90) | 25 | 0.15 | - | 1.52 |
| | 3 | Ol7.4, Pl41.41, Cpx48.27, Ox2.7 Sulfide0.22 (Fe-S 85, Cu-Fe-S 15) | 25 | 0.15 | - | 1.91 |
| | 4 | Ol5.2, Pl43.71, Cpx38.67, Ox12.2 Sulfide0.22 (Fe-S 85, Cu-Fe-S 15) | 25 | 0.15 | - | 2.00 |
| | 5, $VE_{1,A}$ | Ol5.4, Pl41.6, Cpx46.0, Ox2.7 Fluid4.3 | 25 | 0.15 | 5 | **1.40** |
| | 5, $VE_{1,B}$ | Ol5.4, Pl41.6, Cpx45.78, Ox2.7 Sulfide0.22 (Fe-S 10, Cu-Fe-S 90) Fluid4.3 | 25 | 0.15 | 5 | 1.52 |
| | 5, $VE_{1,C}$ | Ol5.4, Pl41.6, Cpx45.78, Ox2.7 Sulfide0.22 (Fe-S 85, Cu-Fe-S 15) Fluid4.3 | 25 | 0.15 | 5 | 1.57 |
| | 5, $VE_{1,D}$ | Ol4.2, Pl41.98, Cpx37.1, Ox12.2 Sulfide0.22 (Fe-S 85, Cu-Fe-S 15) Fluid4.3 | 25 | 0.15 | 5 | 2.00 |
| | 5, $VE_{2,A}$ | Ol6.0, Pl40.81, Cpx46.97, Ox2.7 Sulfide0.22 (Fe-S 85, Cu-Fe-S 15) Fluid3.3 | 25 | 0.15 | 4 | **1.55** |
| | 5, $VE_{2,B}$ | Ol6.0, Pl40.81, Cpx46.97, Ox2.7 Sulfide0.22 (Fe-S 85, Cu-Fe-S 15) Fluid3.3 | 25 | 0.15 | 4 | 1.71 |
| | 5, $VE_{2,C}$ | Ol4.6, Pl42.18, Cpx37.5, Ox12.2 Sulfide0.22 (Fe-S 85, Cu-Fe-S 15) Fluid3.3 | 25 | 0.15 | 4 | 2.00 |
| | 5, $VE_{3,A}$ | Ol7.0, Pl40.81, Cpx46.87, Ox2.7 Sulfide0.22 (Fe-S 85, Cu-Fe-S 15) Fluid2.4 | 25 | 0.15 | 3 | **1.85** |
| | 5, $VE_{3,B}$ | Ol5.0, Pl42.5, Cpx37.68, Ox12.2 Sulfide0.22 (Fe-S 85, Cu-Fe-S 15) Fluid2.4 | 25 | 0.15 | 3 | 2.00 |

| | 5, VE$_4$ | Ol5.2, Pl42.8, Cpx38.08, Ox12.2 Sulfide0.22 (Fe-S 85, Cu-Fe-S 15) Fluid1.5 | 25 | 0.15 | 2 | **2.20** |
|---|---|---|---|---|---|---|

265

| | Silicate melt composition | Cu | Pd | Zn | Pb | Co |
|---|---|---|---|---|---|---|
| $D_{olvine-SM}$ | B to BA | 0.023[20] | 0.005[22,23] | 0.8[20] | 0.0001[24] | 4.3[20] |
| | BA to D | 0.1325[21] | | 1.2[21] | 0.0108[25] | 6.41[26] |
| $D_{plagioclase-SM}$ | B to BA | 0.17[27] | 0.2[28-30] | 0.18[27] | 0.666[31] | 0.026[32] |
| | BA to D | 0.16[28] | | 0.17[28] | 0.625[25] | 0.07[33] |
| $D_{clinopyroxene-SM}$ | B to BA | 0.071[34] | 0.3[28-30,35-37] | 0.5[34] | 0.0102[38] | 1.32[34] |
| | BA to D | 0.065[21] | | 0.275[21] | 0.0102[38] | 1.2[21] |
| $D_{oxide-SM}$ | B to BA | 0.42[39] | 1.1[28,29,41] | 2.6[40] | 0.0001 | 3.4[39] |
| | BA to D | 0.15[40] | | 5.4[42] | | 21[43] |
| $D_{CuFeS-SM}$ | B to D | 1,600[44] and references therein * | 8,000[45-48] and references therein *** | 4.5 (1.2 to 19)[44] and references therein ** | 30[44] and references therein * | 24 (B to BA) 96 (BA to D)[44]**** |
| $D_{FeS-SM}$ | B to D | 1,000[44] and references therein * | 0.2x$D_{CuFeS-SM}$(Pd)[49] | 1.5 (0.6 to 2.9)[44] and references therein ** | 0.15[44] and references therein ** | 56 (B to BA) 188 (BA to D)[44] and references therein **** |
| $D_{AF-SM}$ | B to D | 10 to 100[50-53] ***** | 0.01x$D_{AF-SM}$(Cu)[54] | 3.7 (2.3 to 5)[52] | 9.9 (8.4 to 15)[52] | 0.0001 |

271 * average value for samples with temperatures between 1100-1200°C and with FeO concentrations

272 between 4-12 wt.%.

273 ** average value for all the samples presented.

274 *** Based on the evolution of Pd in the Niuatahi Motutahi[46] and the Eastern Manus Back-arc Basin[45], the

275 value of $D_{CuFeS-SM}$ for Pd was estimated to 10,000[47]. On the other hand, another study determined

276 experimentally that the $D_{CuFeS-SM}$ of Pd is equal to 4,000[48]. While using a value of 4,000 for the $D_{CuFeS-SM}$ of

277 Pd leads to an overestimation of the calculated Pd values in group 1A, using the value of 10,000 forces us

278    to use Fe-S:Cu-Fe-S proportion of 99:1, which contradicts the observation of ~15:85 observed on some

279    sulfides identified in group 1A (e.g., Supplementary Figure 4, 5). Hence, we opted for a $D_{CuFeS-SM}$ value of

280    8,000 for Pd, striking a compromise that allows matching between measured and calculated values for

281    group 1A while maintaining consistent Fe-S:Cu-Fe-S proportions. This value was consistently applied to

282    group 1B(a) as well.

283    **** Since $D_{CuFeS-SM}$ and $D_{FeS-SM}$ for Co are significantly influenced by the composition of the silicate liquid

284    compared to Cu, Zn and Pb, we used the averaged value of partition coefficients estimated from samples

285    with basaltic compositions for Fatu Kapa magmas displaying basaltic to basalt-andesitic compositions and

286    used the partition coefficient of the only sample displaying andesitic composition for Fatu Kapa magmas

287    displaying basalt-andesitic to dacitic compositions.

288    ***** The $D_{AF-SM}$ of Cu is a positive function of the Cl content in the aqueous fluid[53,55,56]. Since group 1B(a)

289    magmas are Cl-rich (Cl ~0.7 wt.%)[10], we used the value of 100 for the $D_{AF-SM}$ of Cu.

290

291    **Supplementary Note 4:** Notes on Experimental Conditions and Natural System Characteristics from which

292    Used Partition Coefficients are Calculated.

293    <u>Silicate minerals-silicate melt and oxide-silicate melt partition coefficients</u>

294    [20] Natural system. Reduced basaltic dike (Disko Island, Greenland).

295    [21] Natural system. Island arc suites from basalts to dacites (St. Vincent Island, La Soufrière volcano, West

296    Indies).

297    [22] Experimental. Iron-bearing basalt at 0.001 kbar with a $fO_2$ at 4.3 and 2.0 log units above the fayalite-

298    magnetite-quartz buffer and 0.5 below this buffer.

299    [23] Experimental. Synthetic basalt oxide mixture at 1260-1350°C, 0.001 kbar with a $fO_2$ from 0.6 to 5.4 log

300    units above the fayalite-magnetite-quartz buffer.

301    [24] Natural systems. Worldwide mid-ocean ridge and ocean-island basalts.

302    [25] Natural system. Continental arc suites from alkali olivine basalts to andesites (Mt. Adams, Cascade

303    Range, USA).

304    [26] Natural system. Magmatic series consisting of trachybasalts, latites and trachyphonolites (Phlegrean

305    Fields, Central Italy).

306    [27] Natural system. Basalts (Tolbachik, Kamtchatka, Russia).

307    [28] Natural systems. Worldwide orogenic and non-orogenic leucitic and picritic basalts to high-silica and

308    peralkaline rhyolites.

309    [29] Experimental. $CaO$-$MgO$-$SiO_2$-$Al_2O_3$-$FeO$-$TiO_2$ synthetic system at 1250 to 1510°C, 0.001 kbar with a $fO_2$

310    from 3.5 to 0 log units below the fayalite-magnetite-quartz buffer.

311    [30] Natural system. Large igneous provinces basalts from Ocean Drilling Program Leg 183 (Kerguelen

312    Plateau, Southern Indian Ocean).

313    [31] Experimental. Synthetic albite and anorthite added to natural basaltic andesite samples at 0.001 kbar.

314    [32] Natural system. Gabbros from a layered series (Skaergaard intrusion, East Greenland).

315    [33] Natural setting. Andesites and rhyolites from a calcalkaline series (Mount Mazama, Crater Lake, USA).

316    [34] Natural setting. Mid-ocean ridge basalts (Rift Valley, Atlantic Ocean).

317    [35] Experimental. $CaO$-$MgO$-$SiO_2$-$Al_2O_3$ synthetic system at 1300°C and 1450°C and 0.001 kbar.

318    [36] Experimental. $Na_2O$–$CaO$–$MgO$–$Al_2O_3$–$SiO_2$ synthetic system at 1218°C and 0.001 kbar.

319   [37] Experimental. Hawaiian ankaramite, synthetic eucrite basalt and a diopside-anorthitic eutectic melt at

320   0.001 kbar, 19 kbar and 20 kbar, respectively, and at a temperature of 1200-1300°C and $fO_2$ between the

321   nickel-nickel-oxide and hematite-magnetite buffers.

322   [38] Primitive alumina basalt at 1405°C and 17 kbar with a $fO_2$ equal to the carbon-carbon monoxide-carbon

323   dioxide buffer.

324   [39] Natural systems. Basaltic to trachytic lavas from alkaline series (Velay, Chaîne des Puys: Massif Central,

325   France and Fayal: Azores).

326   [40] Natural setting. Basalt-andesite (Colorado Plateau, USA).

327   [41] Experimental. Spinels equilibrated with natural and synthetic iron-bearing basalt at 1400-1900°C, 0.001

328   kbar with a $fO_2$ range of 1.6 to 7.0 log units above the iron-wüstite buffer.

329   [42] Natural setting. Andesites (Colima volcanic complex, Mexico).

330   [43] Natural setting. Trachytes to pantellerites (Fe-rich peralkaline felsic rock) (Pantelleria, Straight of Sicily).

331   <u>Sulfide liquid-silicate melt and monosulfide solid solution-silicate melt partition coefficients</u>

332   [44] Experimental. Hydrous basaltic to dacitic melts at 1000-1200°C, 5-10 kbar with an $fO_2$ at 1-1.5 log units

333   above the fayalite-magnetite-quartz buffer.

334   [45] Natural system. PGE behavior from basalts to dacites in the Pual Ridge back-arc system (Manus, Papua

335   New Guinea).

336   [46] Natural system. Cu and PGE behavior from basalts to dacites in the Niuatahi-Motutahi back-arc system

337   (Tonga rear arc).

338   [49] Experimental. Synthetic starting material at 860-926°C, 0.001 kbar with an $fO_2$ controlled by the fayalite-

339   magnetite-quartz buffer.

340   <u>Aqueous fluid-silicate melt partition coefficients</u>

341   [50] Experimental. Aqueous fluid saturated granitic melt at 750°C, 1.4 kbar with Cl- and HF- bearing fluids.

342   [51] Experimental. Aqueous fluid saturated haplogranitic melt at 750°C, 2 kbar with Cl- and HF- bearing fluids.

343   [52] Natural systems. Aqueous fluid saturated granitic melts with temperatures of ~700°C, pressures

344   between ~1.0 to 1.8 kbar and displaying various chlorinity.

345   [53] Experimental. Aqueous fluid saturated basaltic melt at 850°C, 2 kbar with Cl- bearing fluids.

346   [54] Natural system. Comparison of the PGE and Cu content between altered dacitic lavas and native sulfur

347   condensates in a fore-arc system (Niuatahi-Motutahi, Tonga rear arc).

348
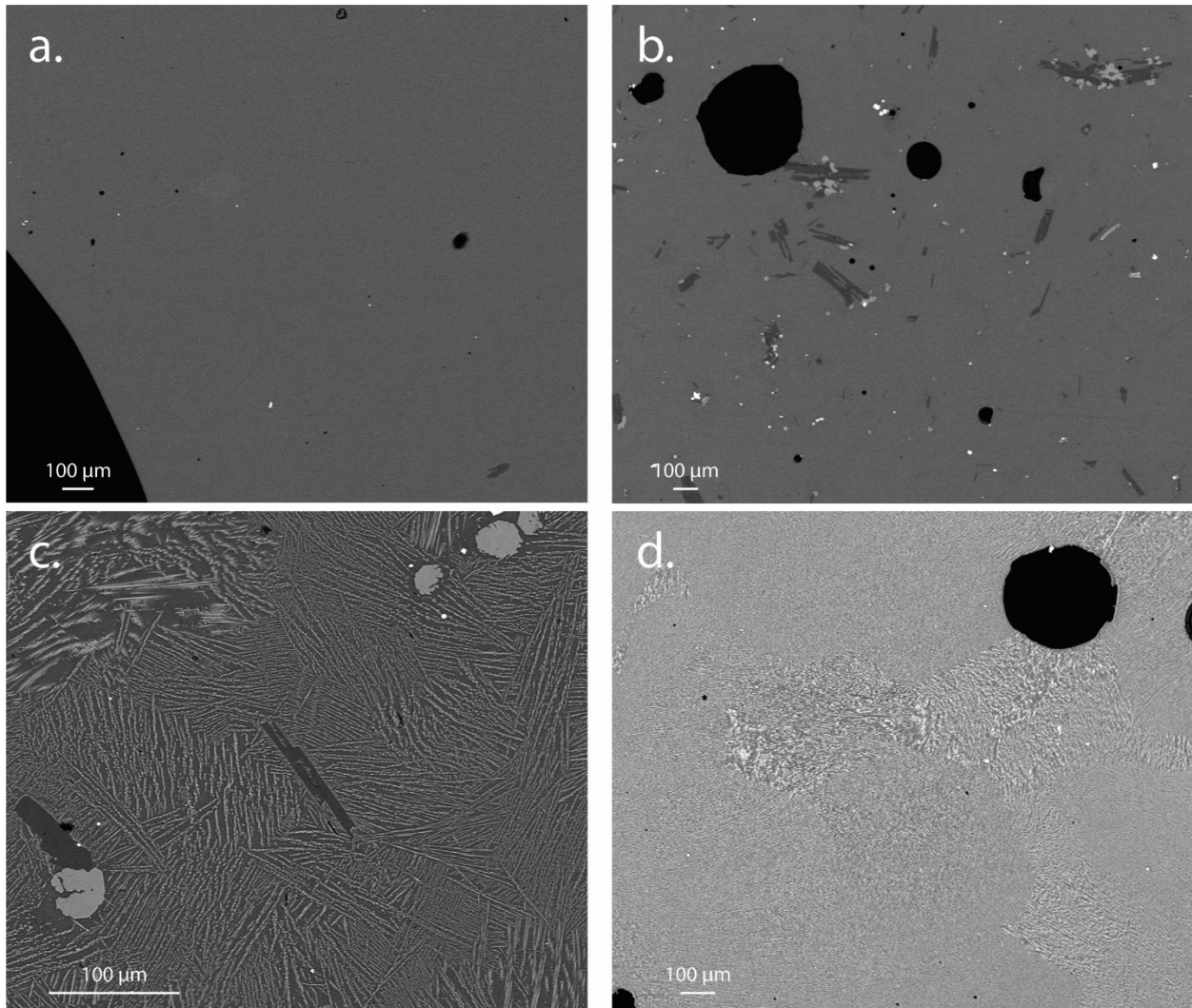
**Supplementary Figure 12:** SEM images of group 1B(a) lavas. **a.** Aphyric trachydacite displaying almost no silicate phases (sample FU3-PL-03-03). **b.** Aphyric trachydacite displaying ~10 % of silicate phases (sample FU2-DR-27-05). Silicate phases include plagioclases (darker plurimicrometric phases) and clinopyroxenes (lighter plurimicrometric phases). White micrometric phases are oxides. **c.** Aphyric trachyandesite displaying ~5 % of silicate phases (sample FU3-DR-05-01). Silicate phases are the same as in b. Note the glassy texture visible at this scale. **d.** Aphyric trachydacite displaying no silicate phases (sample FU3-DR-06-01). Devitrification textures are observed in the glass.

356 **Supplementary Table 6:** Cu and Pb measurements of the reference materials NIST SRM 614 (NIST614,

357 synthetic)[57], BCR2g (basalt)[58], BIR1g (basalt)[58] by LA-ICPMS. The standard deviation (ppm) is calculated

358 with the equation $2\sigma = 2\sqrt{\dfrac{2\sum(x-\bar{x})^2}{n(n-1)}\dfrac{\bar{x}_{corr}}{\bar{x}}}$ where $x$ represents the intensity of the element measured at a

359 given time, $\bar{x}$ stands for the intensity of the element averaged for the time used to estimate the

360 concentration of the element, n is the number of signals recorded, and $\bar{x}_{corr}$ is the estimated

361 concentration of the element. Certified values are highlighted in bold.

| Sample analysed | Cu BIR1g | $2\sigma$ | Cu BCR2g | $2\sigma$ | Cu NIST614 | $2\sigma$ | Pb BIR1g | $2\sigma$ | Pb BCR2g | $2\sigma$ | Pb NIST614 | $2\sigma$ |
|---|---|---|---|---|---|---|---|---|---|---|---|---|
| Ref. | **119** | **24** | **21.0** | **10.0** | **1.37** | **0.14** | **3.70** | **0.60** | **11.0** | **2.0** | **2.32** | **0.08** |
| FU3DR0106 | 139 | 8 | - | - | 1.03 | 0.29 | 3.71 | 0.39 | - | - | 2.42 | 0.14 |
| FU3DR0107 | 134 | 9 | - | - | 1.35 | 0.32 | 3.68 | 0.30 | - | - | 2.45 | 0.22 |
| FU3DR0304 | 136 | 6 | - | - | 0.97 | 0.24 | 3.87 | 0.22 | - | - | 2.08 | 0.08 |
| FU3DR0501 | 131 | 7 | - | - | 0.87 | 0.34 | 3.82 | 0.21 | - | - | 2.40 | 0.20 |
| FU3DR0601 | 124 | 6 | - | - | 1.01 | 0.33 | 3.52 | 0.15 | - | - | 2.33 | 0.16 |
| FU3PL0302 | 131 | 5 | - | - | 1.94 | 1.42 | 3.56 | 0.16 | - | - | 2.65 | 0.59 |
| FU3PL0303 | 128 | 5 | - | - | 1.30 | 0.23 | 3.70 | 0.15 | - | - | 2.19 | 0.13 |
| FU2DR2703 | - | - | 18.0 | 1.0 | - | - | - | - | 10.5 | 0.7 | - | - |
| FU2DR2705 | 126 | 4 | | | 1.18 | 0.31 | 3.60 | 0.17 | | | 2.35 | 0.16 |
| FU2DR2604 | 124 | 8 | 13.8 | 1.1 | 1.75 | 1.03 | 3.58 | 0.25 | 9.4 | 0.5 | 2.24 | 0.30 |
| FU3DR0108 | 136 | 9 | 17.9 | 1.9 | 0.57 | 0.98 | 3.81 | 0.24 | 11.9 | 1.4 | 2.63 | 0.20 |
| FU3DR0109 | 135 | 5 | 15.2 | 0.9 | 1.31 | 1.19 | 3.56 | 0.21 | 10.3 | 0.4 | 2.27 | 0.20 |
| FU3DR1304 | 133 | 4 | 17.7 | 2.0 | 2.28 | 1.30 | 3.41 | 0.18 | 10.5 | 0.3 | 3.59 | 0.31 |
| FU3DR1305 | 134 | 4 | 16.8 | 1.0 | 0.78 | 1.81 | 3.46 | 0.17 | 10.6 | 0.5 | 2.36 | 0.25 |
| FU3DR1503 | 134 | 6 | 16.3 | 2.2 | 0.08 | 1.36 | 3.48 | 0.22 | 10.8 | 0.5 | 2.19 | 0.19 |
| FU2DR1502 | 124 | 10 | 16.7 | 1.3 | 0.43 | 0.45 | 3.52 | 0.51 | 10.6 | 0.8 | 2.46 | 0.20 |
| FU2DR1503 | 128 | 8 | 17.7 | 0.8 | 1.20 | 0.48 | 3.83 | 0.27 | 10.2 | 0.7 | 2.57 | 0.31 |
| FU3DR0306 | 126 | 4 | 17.2 | 0.8 | 0.82 | 0.34 | 3.42 | 0.22 | 10.0 | 0.5 | 2.26 | 0.14 |

362

363     **Supplementary Table 7:** Procedural blank values (n = 18) used to correct the Pd values measured by NIS-

364     FA-ID and to calculate the method detection limit for Pd.

| Date | Pd (ng) | Sample mass (g) |
|---|---|---|
| 23/11/2018 | 0.198 | 5 |
| 23/11/2018 | 0.313 | 5 |
| 07/06/2019 | 0.247 | 5 |
| 07/06/2019 | 0.159 | 5 |
| 07/06/2019 | 0.168 | 5 |
| 11/07/2019 | 0.188 | 5 |
| 11/07/2019 | 0.258 | 5 |
| 06/02/2020 | 0.313 | 5 |
| 21/02/2020 | 0.168 | 5 |
| 10/06/2020 | 0.079 | 5 |
| 29/01/2021 | 0.175 | 5 |
| 23/03/2022 | 0.174 | 5 |
| 23/03/2022 | 0.189 | 5 |
| 23/03/2022 | 0.211 | 5 |
| 16/06/2022 | 0.108 | 5 |
| 16/06/2022 | 0.055 | 5 |
| 16/09/2022 | 0.164 | 5 |
| 16/09/2022 | 0.110 | 5 |

365

366     **Supplementary Table 8:** Pd measurements of the reference material TDB-1 by Ni-sulfide fire assay-isotope

367     dilution. Certified value is highlighted in bold.

| Sample | Pd (ppb) | σ (ppb) |
|---|---|---|
| TDB-1 certified value[59] | **24.3** | **1.9** |
| TDB-1_1 | 23.4 | 0.3 |
| TDB-1_2 | 24.7 | 0.4 |
| TDB-1_3 | 24.1 | 0.4 |
| TDB-1_4 | 23.1 | 0.3 |
| TDB-1_5 | 22.8 | 0.6 |
| TDB-1_6 | 23.6 | 1.0 |

368

# References (Supplementary Information)

1. Hannington, M. D. Geochemical and Tectonic Evolution of Arc-Backarc Hydrothermal Systems: Implication for Origin of Kuroko and Epithermal Vein-type Mineralizations and the Global Geochemical Cycle (N. Shikazono). *Economic Geology* **99**, 1247-1247 (2004).

2. Hannington, M. D., De Ronde, C. E., & Petersen, S. Sea-floor tectonics and submarine hydrothermal systems (2005).

3. Fouquet, Y., Charlou, J. L., von Stackelberg, U., Wiedicke, M., Erzinger, J., Herzig, P. M., & Muehe, R. Metallogenesis in back-arc environments: the Lau Basin example. Economic Geology **88** (1993).

4. Fouquet, Y., Knott, R., Cambon, P., Fallick, A., Rickard, D., & Desbruyeres, D. Formation of large sulfide mineral deposits along fast spreading ridges. Example from off-axial deposits at 12 43′ N on the East Pacific Rise. *Earth and Planetary Science Letters* **144**, 147-162 (1996).

5. Fouquet, Y., Cambon, P., Etoubleau, J., Charlou, J. L., Ondréas, H., Barriga, F. J., ... & Rouxel, O. Geodiversity of hydrothermal processes along the Mid-Atlantic Ridge and ultramafic-hosted mineralization: A new type of oceanic Cu-Zn-Co-Au volcanogenic massive sulfide deposit. *Diversity of hydrothermal systems on slow spreading ocean ridges* **188**, 321-367 (2010).

6. Bendel, V., Fouquet, Y., Auzende, J. M., Lagabrielle, Y., Grimaud, D., & Urabe, T. The White Lady hydrothermal field, North Fiji back-arc basin, southwest Pacific. *Economic Geology* **88**, 2237-2245 (1993).

7. Bézos, A., & Humler, E. The Fe3+/ΣFe ratios of MORB glasses and their implications for mantle melting. *Geochimica et Cosmochimica Acta* **69**, 711-725 (2005).

8. Bézos, A., Guivel, C., La, C., Fougeroux, T., & Humler, E. Unraveling the confusion over the iron oxidation state in MORB glasses. *Geochimica et Cosmochimica Acta* **293**, 28-39 (2021).

391  9.  Kullerud, G., Yund, R. A., & Moh, G. H. Phase relations in the Cu-Fe-S, Cu-Ni-S, and Fe-Ni-S systems.

392     *Economic Geology Monograph* **1** (1969).

393  10. Jeanvoine, A., Chazot, G., Labanieh, S., Pelleter, E., & Fouquet, Y. Origin and evolution of the Fatu

394     Kapa magmatic system (North-Western Lau Back-Arc Basin): insight on the genesis of high-silica

395     lavas. *Journal of Petrology* **62**, egab039 (2021).

396  11. Putirka, K., Johnson, M., Kinzler, R., Longhi, J., & Walker, D. Thermobarometry of mafic igneous

397     rocks based on clinopyroxene-liquid equilibria, 0–30 kbar. *Contributions to Mineralogy and*

398     *Petrology* **123**, 92-108 (1996).

399  12. Putirka, K. D. Thermometers and barometers for volcanic systems. *Reviews in mineralogy and*

400     *geochemistry* **69**, 61-120 (2008).

401  13. Lange, R. A., Frey, H. M., & Hector, J. A thermodynamic model for the plagioclase-liquid

402     hygrometer/thermometer. *American Mineralogist* **94**, 494-506 (2009).

403  14. Waters, L. E., & Lange, R. A. An updated calibration of the plagioclase-liquid hygrometer-

404     thermometer applicable to basalts through rhyolites. *American mineralogist* **100**, 2172-2184

405     (2015).

406  15. Jorgenson, C., Higgins, O., Petrelli, M., Bégué, F., & Caricchi, L. A Machine Learning-Based

407     Approach to Clinopyroxene Thermobarometry: Model Optimization and Distribution for Use in

408     Earth Sciences. *Journal of Geophysical Research: Solid Earth* **127**, e2021JB022904 (2022).

409  16. Wang, X., Hou, T., Wang, M., Zhang, C., Zhang, Z., Pan, R., ... & Zhang, H. A new clinopyroxene

410     thermobarometer for mafic to intermediate magmatic systems. *European Journal of Mineralogy*

411     **33**, 621-637 (2021).

412  17. Jenner, F. E., & O'Neill, H. S. C. Analysis of 60 elements in 616 ocean floor basaltic glasses.

413     *Geochemistry, Geophysics, Geosystems* **13** (2012).

414    18. Ersoy, E. Y., Helvaci, C. & Palmer, M. R.. Mantle source characteristics and melting models for the

415        early–middle Miocene mafic volcanism in Western Anatolia: Implications for enrichment

416        processes of mantle lithosphere and origin of K-rich volcanism in post-collisional settings. *Journal*

417        *of Volcanology and Geothermal Research* **198**, 112–128 (2010).

418    19. Wanless, V. D., Perfit, M. R., Ridley, W. I. & Klein, E. Dacite petrogenesis on mid-ocean ridges:

419        evidence for oceanic crustal melting and assimilation. Journal of Petrology **51**, 2377–2410 (2010).

420    20. Klöck, W., & Palme, H. Partitioning of siderophile and chalcophile elements between metal, sulfide,

421        olivine, and glass in a naturally reduced basalt from Disko Island, Greenland. *Lunar and Planetary*

422        *Science Conference* **18** (1987).

423    21. Dostal, J., Dupuy, C., Carron, J. P., De Kerneizon, M. L. G., & Maury, R. C. Partition coefficients of

424        trace elements: application to volcanic rocks of St. Vincent, West Indies. *Geochimica et*

425        *Cosmochimica Acta* **47**, 525-533 (1983).

426    22. Brenan, J. M., McDonough, W. F., & Dalpe, C. Experimental constraints on the partitioning of

427        rhenium and some platinum-group elements between olivine and silicate melt. *Earth and*

428        *Planetary Science Letters* **212**, 135-150 (2003).

429    23. Brenan, J. M., McDonough, W. F., & Ash, R. An experimental study of the solubility and partitioning

430        of iridium, osmium and gold between olivine and silicate melt. *Earth and Planetary Science Letters*

431        **237**, 855-872 (2005).

432    24. McKenzie, D. A. N., & O'nions, R. K. Partial melt distributions from inversion of rare earth element

433        concentrations. *Journal of Petrology* **32**, 1021-1091 (1991).

434    25. Dunn, T., & Sen, C. Mineral/matrix partition coefficients for orthopyroxene, plagioclase, and

435        olivine in basaltic to andesitic systems: a combined analytical and experimental study. *Geochimica*

436        *et Cosmochimica Acta* **58**, 717-733 (1994).

437    26. Villemant, B. Trace element evolution in the Phlegrean Fields (Central Italy): fractional

438        crystallization and selective enrichment. *Contributions to Mineralogy and Petrology* **98**, 169-183

439        (1988).

440    27. Kravchuk, I. F. Energetics, thermodynamics, and stability of olivine and pyroxene solid solutions.

441        *Geochemistry International* **18**, 158 (1981).

442    28. Ewart, A., & Griffin, W. L. Application of proton-microprobe data to trace-element partitioning in

443        volcanic rocks. *Chemical Geology* **117**, 251-284 (1994).

444    29. Capobianco, C. J., & Drake, M. J. Partitioning and solubility of PGEs in oxides and silicates.

445        *Mineralogical Magazine* **58**, 144-145 (1994).

446    30. Chazey, W. J., & Neal, C. R. Platinum-group element constraints on source composition and

447        magma evolution of the Kerguelen Plateau using basalts from ODP Leg 183. *Geochimica et*

448        *Cosmochimica Acta* **69**, 4685-4701 (2005).

449    31. Bindeman, I. N., Davis, A. M., & Drake, M. J. Ion microprobe study of plagioclase-basalt partition

450        experiments at natural concentration levels of trace elements. *Geochimica et Cosmochimica Acta*

451        **62**, 1175-1193 (1998).

452    32. Paster, T. P., Schauwecker, D. S., & Haskin, L. A. The behavior of some trace elements during

453        solidification of the Skaergaard layered series. *Geochimica et Cosmochimica Acta* **38**, 1549-1577

454        (1974).

455    33. Bacon, C. R., & Druitt, T. H. Compositional evolution of the zoned calcalkaline magma chamber of

456        Mount Mazama, Crater Lake, Oregon. *Contributions to Mineralogy and Petrology* **98**, 224-256

457        (1988).

458    34. Bougault, H., & Hekinian, R. Rift valley in the Atlantic Ocean near 36° 50' N: petrology and

459        geochemistry of basaltic rocks. *Earth and Planetary Science Letters* **24**, 249-261 (1974).

460 35. Capobianco, C. J., & Drake, M. J. Partitioning of ruthenium, rhodium, and palladium between

461   spinel and silicate melt and implications for platinum group element fractionation trends.

462   *Geochimica et Cosmochimica Acta* **54**, 869-874 (1990).

463 36. Hill, E., Wood, B. J., & Blundy, J. D. The effect of Ca-Tschermaks component on trace element

464   partitioning between clinopyroxene and silicate melt. *Lithos* **53**, 203-215 (2000).

465 37. Righter, K., Campbell, A. J., Humayun, M., & Hervig, R. L. Partitioning of Ru, Rh, Pd, Re, Ir, and Au

466   between Cr-bearing spinel, olivine, pyroxene and silicate melts. *Geochimica et Cosmochimica Acta*

467   **68**, 867-880 (2004).

468 38. Hauri, E. H., Wagner, T. P., & Grove, T. L. Experimental and natural partitioning of Th, U, Pb and

469   other trace elements between garnet, clinopyroxene and basaltic melts. *Chemical Geology* **117**,

470   149-166 (1994).

471 39. Lemarchand, F., Villemant, B., & Calas, G. Trace element distribution coefficients in alkaline series.

472   *Geochimica et Cosmochimica Acta* **51**, 1071-1081 (1987).

473 40. Esperança, S., Carlson, R. W., Shirey, S. B., & Smith, D. Dating crust-mantle separation: Re-Os

474   isotopic study of mafic xenoliths from central Arizona. *Geology* **25**, 651-654 (1997).

475 41. Brenan, J. M., Finnigan, C. F., McDonough, W. F., & Homolova, V. Experimental constraints on the

476   partitioning of Ru, Rh, Ir, Pt and Pd between chromite and silicate melt: the importance of ferric

477   iron. *Chemical Geology* **302**, 16-32 (2012).

478 42. Luhr, J. F., & Carmichael, I. S. The Colima volcanic complex, Mexico: I. post-caldera andesites from

479   Volcán Colima. *Contributions to Mineralogy and Petrology* **71**, 343-372 (1980).

480 43. Mahood, G. A., & Stimac, J. A. Trace-element partitioning in pantellerites and trachytes.

481   *Geochimica et Cosmochimica Acta* **54**, 2257-2276 (1990).

482    44. Li, Y., Audétat, A., Liu, Z., & Wang, F. Chalcophile element partitioning between Cu-rich sulfide

483        phases and silicate melt and implications for the formation of Earth's continental crust.

484        *Geochimica et Cosmochimica Acta* **302**, 61-82 (2021).

485    45. Park, J. W., Campbell, I. H., & Arculus, R. J. Platinum-alloy and sulfur saturation in an arc-related

486        basalt to rhyolite suite: evidence from the Pual Ridge lavas, the Eastern Manus Basin. *Geochimica*

487        *et Cosmochimica Acta* **101**, 76-95 (2013).

488    46. Park, J. W., Campbell, I. H., Kim, J., & Moon, J. W. The role of late sulfide saturation in the

489        formation of a Cu-and Au-rich magma: insights from the platinum group element geochemistry of

490        Niuatahi–Motutahi lavas, Tonga rear arc. *Journal of Petrology* **56**, 59-81 (2015).

491    47. Hao, H., Park, J. W., & Campbell, I. H. Role of magma differentiation depth in controlling the Au

492        grade of giant porphyry deposits. *Earth and Planetary Science Letters* **593**, 117640 (2022).

493    48. Zhang, M., & Li, Y. (2021). Breaking of Henry's law for sulfide liquid–basaltic melt partitioning of

494        Pt and Pd. *Nature Communications* **12**, 5994.

495    49. Liu, Y., & Brenan, J. Partitioning of platinum-group elements (PGE) and chalcogens (Se, Te, As, Sb,

496        Bi) between monosulfide-solid solution (MSS), intermediate solid solution (ISS) and sulfide liquid

497        at controlled fO2–fS2 conditions. *Geochimica et Cosmochimica Acta* **159**, 139-161 (2015).

498    50. Candela, P. A., & Holland, H. D. The partitioning of copper and molybdenum between silicate melts

499        and aqueous fluids. *Geochimica et Cosmochimica Acta* **48**, 373-380 (1984).

500    51. Keppler, H., & Wyllie, P. J. Partitioning of Cu, Sn, Mo, W, U, and Th between melt and aqueous

501        fluid in the systems haplogranite-H2O− HCl and haplogranite-H2O− HF. *Contributions to*

502        *Mineralogy and Petrology* **109**, 139-150 (1991).

503    52. Zajacz, Z., Halter, W. E., Pettke, T., & Guillong, M. Determination of fluid/melt partition

504        coefficients by LA-ICPMS analysis of co-existing fluid and silicate melt inclusions: Controls on

505        element partitioning. *Geochimica et Cosmochimica Acta* **72**, 2169-2197 (2008).

506  53. Guo, H., & Audétat, A. Transfer of volatiles and metals from mafic to felsic magmas in composite

507      magma chambers: an experimental study. *Geochimica et Cosmochimica Acta* **198**, 360-378 (2017).

508  54. Park, J. W., Campbell, I. H., & Kim, J. Abundances of platinum group elements in native sulfur

509      condensates from the Niuatahi-Motutahi submarine volcano, Tonga rear arc: Implications for PGE

510      mineralization in porphyry deposits. *Geochimica et Cosmochimica Acta* **174**, 236-246 (2016).

511  55. Williams, T. J., Candela, P. A., & Piccoli, P. M. The partitioning of copper between silicate melts

512      and two-phase aqueous fluids: An experimental investigation at 1 kbar, 800 C and 0.5 kbar, 850

513      C. *Contributions to Mineralogy and Petrology* **121**, 388-399 (1995).

514  56. Simon, A. C., Pettke, T., Candela, P. A., Piccoli, P. M., & Heinrich, C. A. Copper partitioning in a

515      melt–vapor–brine–magnetite–pyrrhotite assemblage. *Geochimica et Cosmochimica Acta* **70**,

516      5583-5600 (2006).

517  57. Jochum, K. P., Weis, U., Stoll, B., Kuzmin, D., Yang, Q., Raczek, I., ... & Enzweiler, J. Determination

518      of reference values for NIST SRM 610–617 glasses following ISO guidelines. *Geostandards and

519      Geoanalytical Research* **35**, 397-429 (2011).

520  58. Gao, S., Liu, X., Yuan, H., Hattendorf, B., Günther, D., Chen, L., & Hu, S. Determination of forty-two

521      major and trace elements in USGS and NIST SRM glasses by laser ablation-inductively coupled

522      plasma-mass spectrometry. *Geostandards Newsletter* **26**, 181-196 (2002).

523  59. Meisel, T., & Moser, J. Platinum-group element and rhenium concentrations in low abundance

524      reference materials. *Geostandards and Geoanalytical Research* **28**, 233-250 (2004).